

Multiple Chern bands in twisted MoTe₂ and possible non-Abelian states

Cheng Xu,^{1,2} Ning Mao,³ Tiansheng Zeng,⁴ and Yang Zhang^{1,5}

¹*Department of Physics and Astronomy, University of Tennessee, Knoxville, TN 37996, USA*

²*Department of Physics, Tsinghua University, Beijing 100084, China*

³*Max Planck Institute for Chemical Physics of Solids, 01187, Dresden, Germany*

⁴*Department of Physics, Xiamen University, China*

⁵*Min H. Kao Department of Electrical Engineering and Computer Science, University of Tennessee, Knoxville, Tennessee 37996, USA*

We investigate the moiré band structures and possible even denominator fractional quantum Hall state in small angle twisted bilayer MoTe₂, using combined large-scale local basis density functional theory calculation and continuum model exact diagonalization. Via large-scale first principles calculations at $\theta = 1.89^\circ$, we find a sequence of $C = 1$ moiré Chern bands, in analogy to Landau levels. Constructing the continuum model with multiple Chern bands and uniform Berry curvature in the second moiré band, we undertake band-projected exact diagonalization using unscreened Coulomb repulsion to pinpoint possible $\nu = -3/2$ non-Abelian states across a wide range of twist angles below $\theta = 2.5^\circ$.

Moiré materials based on transition metal dichalcogenides (TMDs) have emerged as a promising domain for exploring novel quantum phenomena [1, 2]. Owing to the substantial effective mass inherent to TMDs valence bands and the persistence of narrow moiré bands across various twist angles, these materials showcase a diverse array of correlated electron states, characterized by pronounced interaction effects, including Mott and charge-transfer insulators [3–10], generalized Wigner crystals [5, 11–17], and quantum anomalous Hall (QAH) effect [18]. Remarkably, recent transport experiments on twisted MoTe₂ have provided unambiguous evidences of both integer and odd-denominator fractional quantum anomalous Hall (QAH and FQAH) effects [19, 20], and the signature for fractional quantum spin Hall effect at hole filling factor $\nu = -3$ [21]. The observations of FQAH were made within a range of fairly large twist angles, specifically $\theta \sim 2.7^\circ - 3.9^\circ$, evidenced through both optical [22] and compressibility [23] measurements, within the first moiré valence band. While the recent experiment on fractional quantum spin Hall (FQSH) effect [21] at small angle $\theta \sim 2.1^\circ$ revealed the remarkable triple quantum spin Hall effects, driving the interest to higher filling factors and small twisted angles.

The realization of fractional quantum anomalous Hall effect not only fundamentally broadens the spectrum of topological phases of matter but also holds promising prospects for harnessing the power of anyons in topological quantum computations at zero magnetic field [24–28]. On the theory side, the fractional Chern insulator (FCI) phases in topological flat band systems has been proposed for over a decade [29–32]. In recent years, within the graphene [33–36] and TMD [37, 38]-based moiré system, theoretical predictions have pointed to such an exotic state at partial filling of the topological moiré flat band at long moiré wavelength. Non-Abelian quantum Hall states such as the possible Moore-Read state [39] at even-denominator filling factor $\nu = 5/2$ has been discussed in Landau level [40]. Under particle-hole symmetry breaking [41, 42] (e.g. Landau level mixing or local

three-body interaction), several numerical studies [43–46] have shown that the Moore-Read Pfaffian (anti-Pfaffian) state with six-fold ground state degeneracies may be favored. Early numerical studies proposed that topological flat band models may host a fermionic non-Abelian Moore-Read state under synthetic three-body interaction [47] or long range dipolar interaction [48]. However, a realistic simulation of such a non-Abelian state in a microscopic lattice model remains challenging. Recent experiment on fractional quantum spin Hall effect [21] indicates the possibility of a time-reversal pair of the even-denominator $3/2$ FQAH states, reveals a strong candidate for the emergence of a non-Abelian state of topological moiré minibands in twisted MoTe₂. Motivated by these developments, we theoretically analyze and propose the realistic conditions for the emergence.

In this work, we start from the local basis first-principle calculations and continuum model at $\theta = 1.89^\circ$, and study the possible non-Abelian state at $\nu = -3/2$, filled to the second moiré valence band. From local basis density functional calculations (DFT), we find the number of $C = 1$ Chern bands increases from 2 [49, 50] to 5 when twist angle changes from $\theta = 5.08^\circ$ to $\theta = 1.89^\circ$. The Chern number of DFT bands are directly calculated from Berry curvature and Wilson loop from DFT wave functions. Moreover, we confirm the multiple $C = 1$ bands from edge states calculations.

For the fitting the continuum model at $\theta = 1.89^\circ$, we constrain the parameter space via fixing the Chern number of top five valence bands and increasing the weight of second moiré bands. With the small angle continuum model, we find strong evidences for the Moore-Read states through momentum-space exact diagonalization spectrum in several different lattice geometries. The ground state degeneracy and momentum locations fulfill the generalized Pauli principle [51, 52] for Moore-Read state [39] for even and odd number of electrons, similar to those in the half-filled first excited Landau level. Our study provides a detailed study of multiple topological bands in twisted MoTe₂ and the continuum model

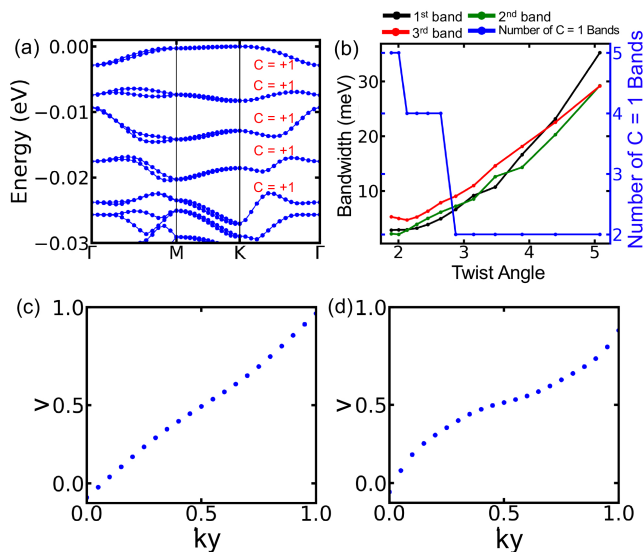


FIG. 1. (a) Band structures for homobilayer MoTe₂ with twist angle 1.89°, where the five flat bands near the Fermi level possess a Chern number of $C = 1$. (b) Angle dependent band width and number of $C = 1$ bands 1.89° to 5.08°, calculated by local-basis DFT. The black, green, and red dotted lines denote for the band width of the first, second, and third band. The blue dotted line represent for the number of $C = 1$ bands. The evolution of Wannier charge center for the (c) first band and (d) second band, indicating that $C = 1$.

for realizing non-Abelian states, paving the way for its materials realizations.

DFT results for twist angle $\theta = 1.89^\circ$. Here we employ the local-basis OpenMX package, utilizing Projected Atomic Orbitals (PAOs) specified as *Mo7.0-s3p2d1* and *Te7.0-s3p2d2* [53, 54]. The real-space Hamiltonian is determined by the hopping strength between different sites, while the overlap parameters are calculated using the PAOs as follows:

$$\begin{aligned} H_{i\alpha,j\beta} &= \sum_n \langle \phi_{i\alpha}(\mathbf{r} - \tau_i) | \hat{H} | \phi_{j\beta}(\mathbf{r} - \tau_j - \mathbf{R}_n) \rangle \\ S_{i\alpha,j\beta} &= \sum_n \langle \phi_{i\alpha}(\mathbf{r} - \tau_i) | \phi_{j\beta}(\mathbf{r} - \tau_j - \mathbf{R}_n) \rangle \end{aligned} \quad (1)$$

where i, j, α , and β represent atom and orbital indices, τ_j and \mathbf{R}_n denote for the atomic and lattice position. Then, the eigenvalues $E_{n\gamma}$ and eigen-vectors $v_{n\gamma,j\beta}$ can be determined by the generalized eigenvalue problem:

$$\sum_{j\beta} (H_{i\alpha,j\beta} - E_{n\gamma} S_{i\alpha,j\beta}) v_{n\gamma,j\beta} = 0 \quad (2)$$

For simplicity, we rewrite the eigen-vectors $v_{n\gamma,j\beta}$ as $|v_n(\mathbf{k})\rangle$. The PBE exchange-correlation functional and the norm-conserving pseudopotential [55] are employed in the calculation with single Γ k -sampling, and we set the convergence criterion as 6×10^{-5} Hartree. For the twist angle of 1.89°, there are 1838 Mo atoms and 3676 Te atoms, forming a Hamiltonian with 191152 dimensions

[56]. Since full diagonalization of such a Hamiltonian is unrealistic in present hardware platform, we apply the shift-and-invert trick, recasting the generalized eigenvalues problem to the eigenvalues problem, and then apply the Lanczos algorithm to get part of the eigenvalues near Fermi level as commonly used in linear-scaling DFT [57, 58].

In twisted MoTe₂, the twist angle emerges as a degree of freedom for manipulating the electronic structures. As shown in Fig. 1, our DFT calculations demonstrate a clear trend: a decrease in the twist angle leads to a reduction in the bandwidth near the Fermi level. For a relatively large twist angle of 5.08°, the smallest bandwidth is 29 meV for the second band, consistent with plane-wave DFT [50, 56]. However, at the small twist angle of 1.89°, five nearly flat bands emerge near the Fermi level, with a small bandwidth of 2.9, 2.2, 5.3, 3.7, and 4.6 meV, respectively. As a result of C_{2y} symmetries, bands along the ΓK lines are doubly degenerate, while a clear splitting is observed along the ΓM line as shown in Fig. 1(a). Furthermore, our results show multiple band inversions near a twist angle of 1.89°, leading to the formation of topological flat bands. These bands are distinctively separated from others by a band gap ranging from 1.9 meV to 3.9 meV. The band separation hints at the possibility of various QSH states [21], including single, double, triple QSH states, with increased hole doping in the system.

With twisted Hamiltonian, we then proceed to study the topological properties of narrow bandwidth moiré valence band. We note the previous C_3 symmetry indicator at C_{3z} symmetric momenta can not accurately determine the Chern numbers with modulo three [37]. The precise calculation requires the momentum space integration of Berry curvature or Berry connection. Despite Kramer pairs have a Chern number of zero due to time-reversal symmetry, a significant Berry curvature can still manifest within a single valley. To separate the single valley from the Hamiltonian, we construct the valley operator \hat{s}_z based on the atomic positions and orbital elements, and separate the single-valley eigen-vectors $|u_m(\mathbf{k})\rangle$ from the entire eigen-vectors $|v_m(\mathbf{k})\rangle$ based on the expectation value of \hat{s}_z :

$$S_{mn}^z(\mathbf{k}) = \langle u_m(\mathbf{k}) | \hat{s}_z | u_n(\mathbf{k}) \rangle \quad (3)$$

Across the two-dimensional Brillouin zone, most of the lines—excluding the ΓK and MK lines—are non-degenerate, with their expectation values of \hat{s}_z approaching either +1 or -1. For those lines that are degenerate, a basis transformation is implemented to construct the disentangled wavefunctions, characterized by expectation values of +1 or -1. This allows us to feasibly separate the single-valley eigenvectors from the valley-mixed eigenvectors.

Therefore, the valley Chern number can be calculated by the integral of the Berry curvature for the single-valley eigen-vectors. Due to the large number of atomic orbitals, the Kubo formula approach requiring full diagonalization is inapplicable here. Therefore, we calculate

the Berry curvature distribution $F(\mathbf{k})$ through the Fukui-Hatsugai-Suzuki method [59]:

$$\begin{aligned} U_{\Delta\mathbf{k}}(\mathbf{k}) &= \det \langle u_n(\mathbf{k}) | u_m(\mathbf{k} + \Delta\mathbf{k}) \rangle \\ F(\mathbf{k}) &= \text{Im} \log U_{\Delta k_1}(\mathbf{k}) U_{\Delta k_2}(\mathbf{k} + \Delta k_1) \times \\ &U_{\Delta k_1}^{-1}(\mathbf{k} + \Delta k_2) U_{\Delta k_2}^{-1}(\mathbf{k}), \end{aligned} \quad (4)$$

where $U_{\Delta k_1}(\mathbf{k})$ is the overlap matrix between two neighboring wave vectors, and $u_n(\mathbf{k})$ denote for the single-valley wave function for the n th band. By integrating the Berry curvature over the entire Brillouin zone, the Chern number for a single band can be determined by the formula: $C_n = \frac{1}{2\pi} \int F(\mathbf{k}) dk^2$. As shown in Fig. 2(a), the distribution of Berry curvature is not uniform across the Brillouin zone, highlighting significant topological interest. To further verify the nontrivial characteristics, we also examine the evolution of Wannier charge centers [60, 61]:

$$\nu_n(k_y) = \int \langle u_n(\mathbf{k}) | \partial_{k_x} | u_n(\mathbf{k}) \rangle dk_x \quad (5)$$

As illustrated in Fig. 1(c) and 1(d), the number of crossings between the WCC and any horizontal lines is 1, indicating the Chern number of 1. Furthermore, $C = 1$ for top five moiré bands will lead to the presence of multiple pairs of gapless edge states inside bulk gap. This is clearly illustrated in Fig. S1(b), thereby confirming the topological properties of the flat Chern bands.

Continuum model with high harmonic term. To perform the many-body calculation, we start with the continuum model for twisted MoTe₂ [62]. Here we incorporate the higher-order harmonic terms for both inter-layer and intra-layer coupling, extending up to the second harmonics. Considering the significant momentum difference between the two valleys ($1/a \gg 1/a_m$), we ignore the inter-valley coupling, focusing solely on the K valley. Additionally, we limit our model to single-spin, owing to the large Ising spin-orbit coupling in MoTe₂. As a result, we arrive at the following continuum model for the K valley:

$$\hat{H}_s = \begin{bmatrix} -\frac{(\hat{\mathbf{k}} - \mathbf{K}_t)^2}{2m^*} + \Delta_t(\mathbf{r}) & \Delta_T(\mathbf{r}) \\ \Delta_T^\dagger(\mathbf{r}) & -\frac{(\hat{\mathbf{k}} - \mathbf{K}_b)^2}{2m^*} + \Delta_b(\mathbf{r}) \end{bmatrix} \quad (6)$$

with:

$$\begin{aligned} \Delta_l(\mathbf{r}) &= 2V_1 \sum_{i=1,3,5} \cos(\mathbf{g}_i^1 \cdot \mathbf{r} + l\phi_1) + 2V_2 \sum_{i=1,3,5} \cos(\mathbf{g}_i^2 \cdot \mathbf{r}) \\ \Delta_T &= w_1 \sum_{i=1,2,3} e^{-i\mathbf{q}_i^1 \cdot \mathbf{r}} + w_2 \sum_{i=1,2,3} e^{-i\mathbf{q}_i^2 \cdot \mathbf{r}} \end{aligned} \quad (7)$$

where $\hat{\mathbf{k}}$ is the momentum, $\mathbf{K}_t(\mathbf{K}_b)$ is high symmetry momentum \mathbf{K} of the top(bottom) layer, $\Delta_t(\mathbf{r})(\Delta_b(\mathbf{r}))$ is the layer dependent moiré potential, $l = +1$ for top layer and $l = -1$ for bottom layer; $\Delta_T(\mathbf{r})$ is the inter-layer tunneling, \mathbf{G}_i is moiré reciprocal vector, \mathbf{g}_i^1 and \mathbf{g}_i^2

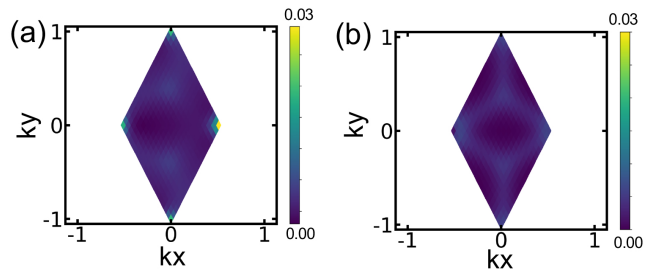


FIG. 2. The Berry curvature distributions across the two-dimensional Brillouin zone for the second band, calculated by (a) first-principles calculations and (b) continuum model. We note the distribution is similarly positive and uniform, and sums to a Chern number of 1.

represent the momentum differences between the nearest and second-nearest plane wave bases within the same layer. Similarly, \mathbf{q}_i^1 and \mathbf{q}_i^2 denote the momentum differences between the nearest and second-nearest plane wave bases across different layers.

To derive the parameters of continuum model, we adopt two guiding principles in the fitting of DFT band structures. Firstly, we ensure that the Chern numbers for top five valence bands are equal to 1, close related to Landau levels [63]. Subsequently, particular focus is placed on the second band, for which we minimize the error of band dispersion and Berry curvature distribution as much as possible. From our DFT calculation at $\theta = 1.89^\circ$, we obtain the parameters as:

$$\begin{aligned} \phi_1 &= -90.0^\circ, V_1 = 2.4 \text{ meV}, V_2 = 1.0 \text{ meV} \\ w_1 &= -5.8 \text{ meV}, w_2 = 2.8 \text{ meV} \end{aligned} \quad (8)$$

The fitting results are shown in Fig. S1(a), where the major topological features are captured in the continuum model. Figure 2(b) displays the distributions of Berry curvature, where both the shape and magnitude closely resemble those obtained from DFT calculations. Additionally, the new parameters effectively capture the variation in the Chern number with the twist angle, as demonstrated in Fig 4.(b), where the top three bands consistently exhibit $C = 1$ within the range of 1° to 3° . It is found that the potential terms are significantly smaller than those derived from the DFT bands at larger twist angle $\theta > 2.89^\circ$ [50, 56, 64, 65]. This difference indicates that the parameters previously employed do not effectively describe the higher moiré valence bands at small twist angles ($\leq 2.5^\circ$).

Exact Diagonalization at $\nu = -3/2$. With the continuum model tailored for $\theta = 1.89^\circ$ and multiple Chern bands, we project the interaction on the second moiré bands, and start with the spontaneous spin polarized assumption to reduce the Hilbert space dimension, which is consistent with large anomalous Hall resistance at small angle devices for filling factor $1 \leq \nu \leq 2$ [21]. The com-

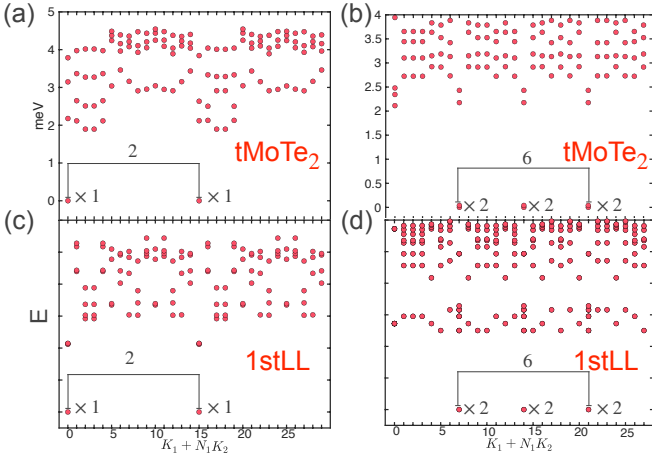


FIG. 3. Exact diagonalization spectrum. (a)/(b) The many-body spectrum from the ED calculation on the 30(28) sites cluster at filling factor $\nu = -\frac{3}{2}$ with the continuum model of MoTe₂ at $\theta = 2.0^\circ$ and we use the dielectric constant $\epsilon = 5$. (c)/(d) The same calculation on the 1st Landau Level, which agrees well with our results from continuum model.

plete many-body Hamiltonian is then expressed as:

$$H = H_s + V, \quad (9)$$

$$V = \sum_{s,s'} \frac{1}{2} \int \int d\mathbf{r}_1 d\mathbf{r}_2 V(\mathbf{r}_1 - \mathbf{r}_2) \hat{c}_s^\dagger(\mathbf{r}_1) \hat{c}_{s'}^\dagger(\mathbf{r}_2) c_{s'}(\mathbf{r}_2) c_s(\mathbf{r}_1)$$

Here, H_s is the single particle continuum model Hamiltonian of hole and V is the Coulomb interaction, $\hat{c}_s^\dagger(\mathbf{r})$ is the creation operator of hole in real space, s is the spin index and we use long range Coulomb interaction: $V(\mathbf{r}_1 - \mathbf{r}_2) = \frac{e^2}{\epsilon|\mathbf{r}_1 - \mathbf{r}_2|}$ and choose the realistic dielectric constant $\epsilon = 5$. We then project the model Hamiltonian into the second moiré valence bands:

$$H_s = \sum_{nks} \epsilon_{nks} a_{nks}^\dagger a_{nks},$$

$$V = \frac{1}{2} \sum_{nsk} V_{n_1 k_1 n_2 k_2 n_3 k_3 n_4 k_4}^{s_1 s_2 s_3 s_4} \hat{a}_{n_1 k_1 s_1}^\dagger \hat{a}_{n_2 k_2 s_2}^\dagger \hat{a}_{n_3 k_3 s_3} \hat{a}_{n_4 k_4 s_4},$$

$$V_{n_1 k_1 n_2 k_2 n_3 k_3 n_4 k_4}^{s_1 s_2 s_3 s_4} = \int \int d\mathbf{r}_1 d\mathbf{r}_2 V(\mathbf{r}_1 - \mathbf{r}_2) \times$$

$$\psi_{n_1 k_1 s_1}^*(\mathbf{r}_1) \psi_{n_2 k_2 s_2}^*(\mathbf{r}_2) \psi_{n_3 k_3 s_3}(\mathbf{r}_2) \psi_{n_4 k_4 s_4}(\mathbf{r}_1) \quad (10)$$

where n is the band index, a_{nks}^\dagger is the creation operator of Bloch states, ψ_{nks} is the eigen-vector of continuum model, $\hat{c}_s^\dagger(\mathbf{r}) = \sum_{nks} \psi_{nks}^*(\mathbf{r}) \hat{a}_{nks}^\dagger$, $\sum_{\mathbf{n}} = \sum_{n_1 n_2 n_3 n_4}$ and so on.

Our calculations focus on the filling $\nu = -3/2$ of single valley for twist angles within the range $\theta \in [1.5^\circ, 2.5^\circ]$, which encompasses experimental twist angles [21]. Our primary findings are depicted in Fig. 3, revealing several quasi-degenerate ground states. Specifically, we identify two-fold quasi-degenerate states for the 30-site cluster (15 electrons), and six-fold degenerate states for the 28-

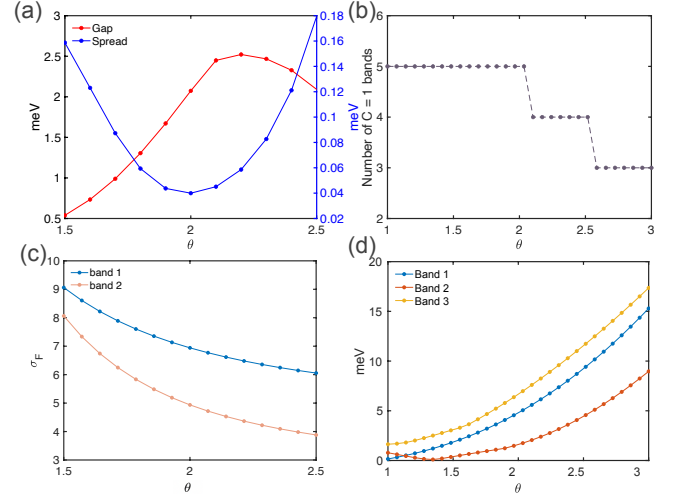


FIG. 4. (a) The red dot denotes the band gap from the ED spectrum, which is defined as the energy difference between the quasi-degenerate states and the excited states. Besides, the blue dot is used to represent the energy spread between the quasi-degenerate ground states. Both data are derived from our ED calculation performed on the 28 sites cluster. (b) The number of bands which have chern number $C = 1$ in the top five moiré bands from the continuum model, it agrees well with the local basis DFT results as we show in Fig.1(b) between $1^\circ \sim 3^\circ$. (c) The fluctuation of Berry curvature of the top two band in the continuum model. (d) The bandwidth of top three moiré bands from the continuum model.

site cluster (14 electrons). Both the momentum location and ground state degeneracy agree well with the requirement of the generalized Pauli principle, where no more than two particles in four consecutive orbitals, called (2,2)-admissible “root” configuration[51, 52]. In short, for an odd number of electrons, the possible (2,2)-admissible “root” configuration [66] requires that only the occupation partition “1010...101010” and its translational invariant partner “0101...010101” are allowed, explaining the two-fold degeneracy. But for even number of electrons, there are six possible configurations, which explain the six-fold degeneracy as demonstrated in the Supplemental Material. The different degeneracies observed for odd and even number of electrons provide compelling evidence suggesting that the ground states may be the Non-Abelian Moore-Read states.

We then perform the twist angle dependent exact diagonalizations. Our analysis reveals that the energy spread between degenerate states reaches a minimum around 2° , while the global gap peaks around 2.2° , as depicted in Figure 4(a). This observation suggests that the system may offer optimal conditions for potential Non-Abelian states at approximately 2° . Moreover, we perform a comparative examination of the states within twisted MoTe₂ and the 1st Landau Level (1st LL), uncovering notable parallels, as depicted in Fig. 3. Additionally, we extend our calculations to clusters of varying sizes, with detailed methodologies outlined in the Supplemental Mate-

rial. Together, these findings underscore the remarkable similarity to the 1st LL across different system configurations.

Given the preservation of particle-hole symmetry in dispersionless Landau levels, the ground states are expected to be symmetrized Moore-Read states, comprising superpositions of Pfaffian and anti-Pfaffian states, owing to potential finite size effects [43, 67, 68]. However, the missing of particle-hole symmetry in our moiré band-projected Hamiltonian would restrict the non-Abelian nature of the ground states at $\nu = -3/2$. Consequently, further investigation is warranted to elucidate the precise nature of the topological order in this context.

Conclusion and outlook. In this study, we investigate the single-particle electronic structures of small-angle moiré MoTe₂ with local basis DFT, exploring its topological properties through Berry curvature and Wilson loop calculations. Specifically, we concentrate on the second moiré band, constructing a continuum model comprising up to five $C = 1$ Chern bands. This model offers insight into various charge fractionalization phenomena reminiscent of those observed in Landau level systems.

Drawing an analogy to the first excited Landau level, our exact diagonalization reveals a remarkably similar many-body spectrum for $\nu = -3/2$ in both even and odd electron systems, providing compelling evidences for the existence of non-Abelian states. We note that in realistic situations, breaking the particle-hole symmetry will lead to the favored Moore-Read Pfaffian. Numerically, the

Pfaffian or anti-Pfaffian nature of the ground states may be distinguished by adding opposite three body interactions, or density-matrix renormalization group calculation of their entanglement spectrum, originating from the different edge structures.

The discovery of integer and fractional quantum Hall effects in the moiré MoTe₂ [19, 20] and pentalayer graphene [69] at zero magnetic field provides ideal material platforms for the realization of charge fractionalization beyond the conventional two-dimensional electron gas at high magnetic field. Similar to a partially filled Landau level, a partially filled topological band can exhibit a symphony of distinct phases as a function of filling factor, each bringing its own novelty as an impetus to extend the frontier of condensed matter physics. While earlier investigations primarily centered on first Chern bands, our study broadens this focus to higher moiré bands, uncovering a series of $C = 1$ bands, laying the foundation for the study of higher filling factor fractional states [21].

Note: Near the completion of this work, we became aware of a related work [70], which studied the non-Abelian state using Skyrminion model and its application in twisted semiconductor bilayers.

ACKNOWLEDGMENTS

We are grateful to Kin Fai Mak, Ahmed Abouelkom-san, Liang Fu, Kai Sun, Zhao Liu for their helpful discussions. Y. Z. is supported by the start-up fund at University of Tennessee Knoxville.

-
- [1] D. M. Kennes, M. Claassen, L. Xian, A. Georges, A. J. Millis, J. Hone, C. R. Dean, D. Basov, A. N. Pasupathy, and A. Rubio, *Nat. Phys.* **17**, 155 (2021).
 - [2] K. F. Mak and J. Shan, *Nature Nanotechnology* **17**, 686 (2022).
 - [3] F. Wu, T. Lovorn, E. Tutuc, and A. H. MacDonald, *Phys. Rev. Lett.* **121**, 026402 (2018), URL <https://link.aps.org/doi/10.1103/PhysRevLett.121.026402>.
 - [4] Y. Zhang, N. F. Q. Yuan, and L. Fu, *Phys. Rev. B* **102**, 201115 (2020), URL <https://link.aps.org/doi/10.1103/PhysRevB.102.201115>.
 - [5] E. C. Regan, D. Wang, C. Jin, M. I. Bakti Utama, B. Gao, X. Wei, S. Zhao, W. Zhao, Z. Zhang, K. Yumigeta, et al., *Nature* **579**, 359 (2020), URL <https://www.nature.com/articles/s41586-020-2092-4>.
 - [6] Y. Tang, L. Li, T. Li, Y. Xu, S. Liu, K. Barmak, K. Watanabe, T. Taniguchi, A. H. MacDonald, J. Shan, et al., *Nature* **579**, 353 (2020), URL <https://www.nature.com/articles/s41586-020-2085-3>.
 - [7] L. Wang, E.-M. Shih, A. Ghiotto, L. Xian, D. A. Rhodes, C. Tan, M. Claassen, D. M. Kennes, Y. Bai, B. Kim, et al., *Nature materials* **19**, 861 (2020).
 - [8] A. Ghiotto, E.-M. Shih, G. S. Pereira, D. A. Rhodes, B. Kim, J. Zang, A. J. Millis, K. Watanabe, T. Taniguchi, J. C. Hone, et al., *Nature* **597**, 345 (2021).
 - [9] T. Li, S. Jiang, L. Li, Y. Zhang, K. Kang, J. Zhu, K. Watanabe, T. Taniguchi, D. Chowdhury, L. Fu, et al., *Nature* **597**, 350 (2021), URL <https://www.nature.com/articles/s41586-021-03853-0>.
 - [10] Y. Xu, K. Kang, K. Watanabe, T. Taniguchi, K. F. Mak, and J. Shan (2022), URL <https://arxiv.org/abs/2202.02055>.
 - [11] Y. Xu, S. Liu, D. A. Rhodes, K. Watanabe, T. Taniguchi, J. Hone, V. Elser, K. F. Mak, and J. Shan, *Nature* **587**, 214 (2020), URL <https://www.nature.com/articles/s41586-020-2868-6>.
 - [12] Y. Zhou, J. Sung, E. Brutschea, I. Esterlis, Y. Wang, G. Scuri, R. J. Gelly, H. Heo, T. Taniguchi, K. Watanabe, et al., *Nature* **595**, 48 (2021), URL <https://www.nature.com/articles/s41586-021-03560-w>.
 - [13] C. Jin, Z. Tao, T. Li, Y. Xu, Y. Tang, J. Zhu, S. Liu, K. Watanabe, T. Taniguchi, J. C. Hone, et al., *Nature Materials* **20**, 940 (2021), URL <https://www.nature.com/articles/s41563-021-00959-8>.
 - [14] H. Li, S. Li, E. C. Regan, D. Wang, W. Zhao, S. Kahn, K. Yumigeta, M. Blei, T. Taniguchi, K. Watanabe, et al., *Nature* **597**, 650 (2021), URL <https://www.nature.com/articles/s41586-021-03874-9>.
 - [15] X. Huang, T. Wang, S. Miao, C. Wang, Z. Li, Z. Lian, T. Taniguchi, K. Watanabe, S. Okamoto, D. Xiao, et al., *Nature Physics* **17**, 715 (2021), URL <https://www.nature.com/articles/s41586-021-03874-9>.

- //www.nature.com/articles/s41567-021-01171-w.
- [16] B. Padhi, R. Chitra, and P. W. Phillips, *Physical Review B* **103**, 125146 (2021).
- [17] M. Matty and E.-A. Kim, *Nature Communications* **13**, 7098 (2022).
- [18] T. Li, S. Jiang, B. Shen, Y. Zhang, L. Li, Z. Tao, T. Devakul, K. Watanabe, T. Taniguchi, L. Fu, et al., *Nature* **600**, 641 (2021), URL <https://www.nature.com/articles/s41586-021-04171-1>.
- [19] H. Park, J. Cai, E. Anderson, Y. Zhang, J. Zhu, X. Liu, C. Wang, W. Holtzmann, C. Hu, Z. Liu, et al., *Nature* **622**, 74 (2023).
- [20] F. Xu, Z. Sun, T. Jia, C. Liu, C. Xu, C. Li, Y. Gu, K. Watanabe, T. Taniguchi, B. Tong, et al., *Physical Review X* **13**, 031037 (2023).
- [21] K. Kang, B. Shen, Y. Qiu, Y. Zeng, Z. Xia, K. Watanabe, T. Taniguchi, J. Shan, and K. F. Mak, *Nature* pp. 1–5 (2024).
- [22] J. Cai, E. Anderson, C. Wang, X. Zhang, X. Liu, W. Holtzmann, Y. Zhang, F. Fan, T. Taniguchi, K. Watanabe, et al., *Nature* pp. 1–3 (2023).
- [23] Y. Zeng, Z. Xia, K. Kang, J. Zhu, P. Knüppel, C. Vaswani, K. Watanabe, T. Taniguchi, K. F. Mak, and J. Shan, *Nature* pp. 1–2 (2023).
- [24] S. A. Parameswaran, R. Roy, and S. L. Sondhi, *C. R. Phys.* **14**, 816 (2013).
- [25] E. J. Bergholtz and Z. Liu, *Int. J. Mod. Phys. B* **27**, 1330017 (2013).
- [26] T. Neupert, C. Chamon, T. Iadecola, L. H. Santos, and C. Mudry, *Phys. Scr.* **2015**, 014005 (2015).
- [27] Z. Liu and E. J. Bergholtz, in *Reference Module in Materials Science and Materials Engineering* (Elsevier, 2023), p. B9780323908009001360, ISBN 978-0-12-803581-8, URL <https://linkinghub.elsevier.com/retrieve/pii/B9780323908009001360>.
- [28] C. Nayak, S. H. Simon, A. Stern, M. Freedman, and S. Das Sarma, *Rev. Mod. Phys.* **80**, 1083 (2008), URL <https://link.aps.org/doi/10.1103/RevModPhys.80.1083>.
- [29] E. Tang, J.-W. Mei, and X.-G. Wen, *Phys. Rev. Lett.* **106**, 236802 (2011), URL <https://link.aps.org/doi/10.1103/PhysRevLett.106.236802>.
- [30] D. Sheng, Z.-C. Gu, K. Sun, and L. Sheng, *Nat. Commun.* **2**, 389 (2011).
- [31] N. Regnault and B. A. Bernevig, *Physical Review X* **1**, 021014 (2011).
- [32] K. Sun, Z. Gu, H. Katsura, and S. D. Sarma, *Physical review letters* **106**, 236803 (2011).
- [33] C. Repellin and T. Senthil, *Physical Review Research* **2**, 023238 (2020).
- [34] P. J. Ledwith, G. Tarnopolsky, E. Khalaf, and A. Vishwanath, *Physical Review Research* **2**, 023237 (2020).
- [35] P. Wilhelm, T. C. Lang, and A. M. Läuchli, *Physical Review B* **103**, 125406 (2021).
- [36] D. Parker, P. Ledwith, E. Khalaf, T. Soejima, J. Hauschild, Y. Xie, A. Pierce, M. P. Zaletel, A. Yacoby, and A. Vishwanath, *arXiv preprint arXiv:2112.13837* (2021).
- [37] T. Devakul, V. Crépel, Y. Zhang, and L. Fu, *Nature communications* **12**, 1 (2021), URL <https://www.nature.com/articles/s41467-021-27042-9>.
- [38] H. Li, U. Kumar, K. Sun, and S.-Z. Lin, *Phys. Rev. Res.* **3**, L032070 (2021).
- [39] G. Moore and N. Read, *Nuclear Physics B* **360**, 362 (1991), ISSN 0550-3213, URL <https://www.sciencedirect.com/science/article/pii/0550321391904070>.
- [40] R. Willett, J. P. Eisenstein, H. L. Störmer, D. C. Tsui, A. C. Gossard, and J. H. English, *Phys. Rev. Lett.* **59**, 1776 (1987), URL <https://link.aps.org/doi/10.1103/PhysRevLett.59.1776>.
- [41] M. Levin, B. I. Halperin, and B. Rosenow, *Phys. Rev. Lett.* **99**, 236806 (2007), URL <https://link.aps.org/doi/10.1103/PhysRevLett.99.236806>.
- [42] S.-S. Lee, S. Ryu, C. Nayak, and M. P. A. Fisher, *Phys. Rev. Lett.* **99**, 236807 (2007), URL <https://link.aps.org/doi/10.1103/PhysRevLett.99.236807>.
- [43] M. R. Peterson, T. Jolicoeur, and S. Das Sarma, *Phys. Rev. Lett.* **101**, 016807 (2008), URL <https://link.aps.org/doi/10.1103/PhysRevLett.101.016807>.
- [44] M. Storni, R. H. Morf, and S. Das Sarma, *Phys. Rev. Lett.* **104**, 076803 (2010), URL <https://link.aps.org/doi/10.1103/PhysRevLett.104.076803>.
- [45] E. H. Rezayi and S. H. Simon, *Phys. Rev. Lett.* **106**, 116801 (2011), URL <https://link.aps.org/doi/10.1103/PhysRevLett.106.116801>.
- [46] K. Pakrouski, M. R. Peterson, T. Jolicoeur, V. W. Scarola, C. Nayak, and M. Troyer, *Phys. Rev. X* **5**, 021004 (2015), URL <https://link.aps.org/doi/10.1103/PhysRevX.5.021004>.
- [47] B. A. Bernevig and N. Regnault, *Phys. Rev. B* **85**, 075128 (2012), URL <https://link.aps.org/doi/10.1103/PhysRevB.85.075128>.
- [48] D. Wang, Z. Liu, W.-M. Liu, J. Cao, and H. Fan, *Phys. Rev. B* **91**, 125138 (2015), URL <https://link.aps.org/doi/10.1103/PhysRevB.91.125138>.
- [49] A. P. Reddy, F. Alsallom, Y. Zhang, T. Devakul, and L. Fu, *Physical Review B* **108**, 085117 (2023).
- [50] C. Xu, J. Li, Y. Xu, Z. Bi, and Y. Zhang, *Proceedings of the National Academy of Sciences* **121**, e2316749121 (2024).
- [51] F. D. M. Haldane, *Physical Review Letters* **67**, 937 (1991).
- [52] B. A. Bernevig and N. Regnault, *Physical Review B* **85**, 075128 (2012).
- [53] T. Ozaki and H. Kino, *Phys. Rev. B* **69**, 195113 (2004).
- [54] T. Ozaki, *Phys. Rev. B* **67**, 155108 (2003).
- [55] I. Morrison, D. M. Bylander, and L. Kleinman, *Phys. Rev. B* **47**, 6728 (1993).
- [56] N. Mao, C. Xu, J. Li, T. Bao, P. Liu, Y. Xu, C. Felser, L. Fu, and Y. Zhang, *arXiv preprint arXiv:2311.07533* (2023).
- [57] D. R. Bowler and T. Miyazaki, *Reports on Progress in Physics* **75**, 036503 (2012).
- [58] Y. Zhang, H. Isobe, and L. Fu, *arXiv preprint arXiv:2005.04238* (2020).
- [59] T. Fukui, Y. Hatsugai, and H. Suzuki, *Journal of the Physical Society of Japan* **74**, 1674 (2005).
- [60] R. Yu, X. L. Qi, A. Bernevig, Z. Fang, and X. Dai, *Phys. Rev. B* **84**, 075119 (2011).
- [61] A. A. Soluyanov and D. Vanderbilt, *Phys. Rev. B* **83**, 035108 (2011).
- [62] F. Wu, T. Lovorn, E. Tutuc, I. Martin, and A. MacDonald, *Phys. Rev. Lett.* **122**, 086402 (2019), URL <https://link.aps.org/doi/10.1103/PhysRevLett.122.086402>.
- [63] N. Morales-Durán, N. Wei, J. Shi, and A. H. MacDonald, *Physical Review Letters* **132**, 096602 (2024).

- [64] Y. Jia, J. Yu, J. Liu, J. Herzog-Arbeitman, Z. Qi, N. Regnault, H. Weng, B. A. Bernevig, and Q. Wu, arXiv preprint arXiv:2311.04958 (2023).
- [65] C. Wang, X.-W. Zhang, X. Liu, Y. He, X. Xu, Y. Ran, T. Cao, and D. Xiao, *Physical Review Letters* **132**, 036501 (2024).
- [66] B. A. Bernevig and F. D. M. Haldane, *Phys. Rev. Lett.* **100**, 246802 (2008), URL <https://link.aps.org/doi/10.1103/PhysRevLett.100.246802>.
- [67] H. Wang, D. N. Sheng, and F. D. M. Haldane, *Phys. Rev. B* **80**, 241311 (2009), URL <https://link.aps.org/doi/10.1103/PhysRevB.80.241311>.
- [68] Z. Zhu, I. Sodemann, D. N. Sheng, and L. Fu, *Phys. Rev. B* **95**, 201116 (2017), URL <https://link.aps.org/doi/10.1103/PhysRevB.95.201116>.
- [69] Z. Lu, T. Han, Y. Yao, A. P. Reddy, J. Yang, J. Seo, K. Watanabe, T. Taniguchi, L. Fu, and L. Ju, *Nature* **626**, 759 (2024).
- [70] A. P. Reddy, N. Paul, A. Abouelkomsan, and L. Fu, arXiv preprint arXiv:2403.00059 (2024).
- [71] L. Zhang, J. Han, H. Wang, R. Car, and E. Weinan, *Phys. Rev. Lett.* **120**, 143001 (2018).

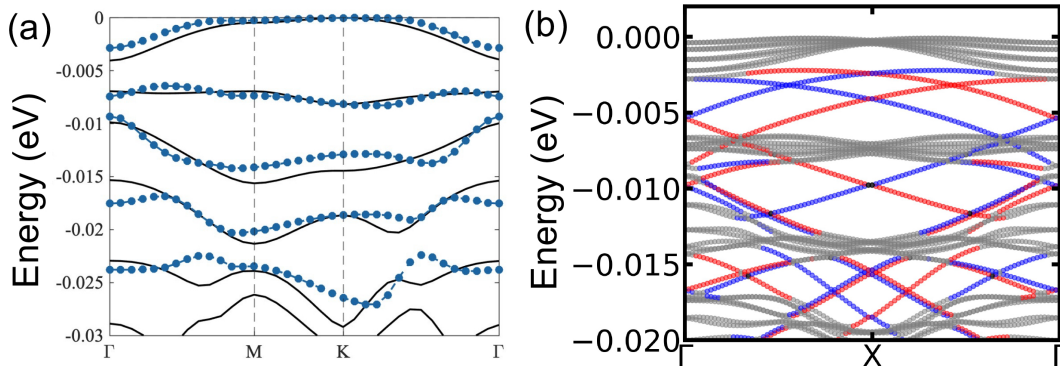


FIG. S1. (a) The comparative analysis of the band structures for twist angle 1.89° . Blue points/lines illustrated the results from OpenMX calculations, while the black line represents the fitting results from continuum model. (b) Band structure of twisted MoTe_2 nanoribbon, calculated from OpenMX hamiltonian. The trivial bulk states are shown in gray, while spin-up/-down edge states are in red/blue.

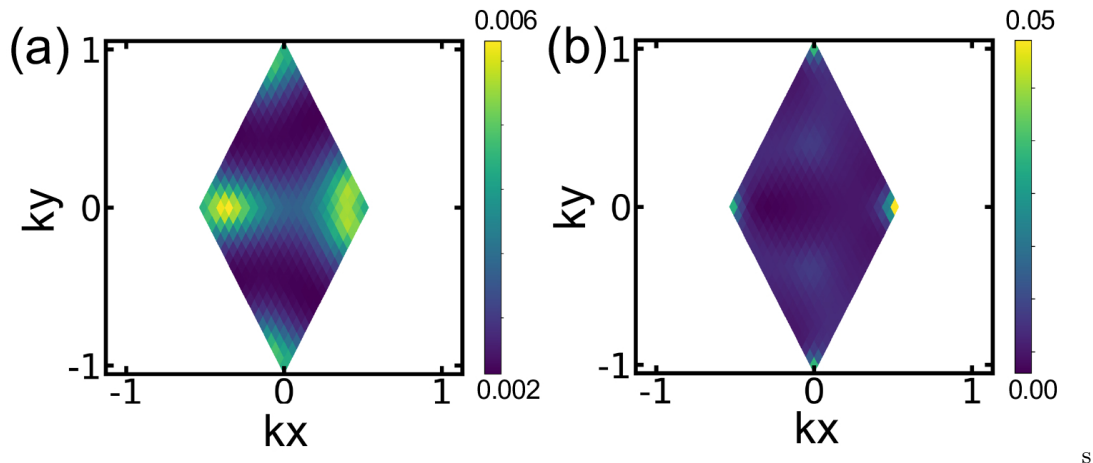


FIG. S2. The DFT Berry curvature distributions of $\theta = 1.89^\circ$ for the (a) top valence band and (b) second valence band.

Appendix

A. Lattice relaxation for homobilayer MoTe_2 with twist angle 1.89°

To relax the structure, we utilize the ab initio deep potential (DP) molecular dynamics method. Our methodology begins with constructing $3 \times 3 \times 1$ MM, MX, and XM configurations and 28 distinct intermediate transition states [71]. Each configuration is relaxed at a fixed volume and then subjected to 200 random perturbations. We then gather initial data sets through 20 fs ab initio molecular dynamics simulations, calculating energies, forces, and virial tensors using VASP. This data set is used to train the DP model, utilizing a descriptor (DeepPot-SE) for both angular and radial atomic configurations and embedding layers mapping descriptors to atomic energies. Following initial training, the model undergoes molecular dynamics simulations across various pressures and temperatures, generating trajectories categorized based on model deviation. Selected configurations undergo self-consistent density functional theory calculations for further training iterations. Furthermore, we expanded our training data with large-angle twisted structures and applied transfer learning principles. By freezing embedding layer parameters and focusing on the hidden and output layers, we construct the transform learning neural network that can be used to relax the homobilayer MoTe_2 with twist angle 1.89° .

Details about openMX calculations. Our openMX basis are Projected Atomic Orbitals (PAOs) specified as $\text{Mo}7.0\text{-}s3p2d1$ and $\text{Te}7.0\text{-}s3p2d2$ [53, 54]. The notation 7.0 indicates a cutoff radius of 7.0 Bohr. For $\text{Mo}7.0\text{-}s3p2d1$,

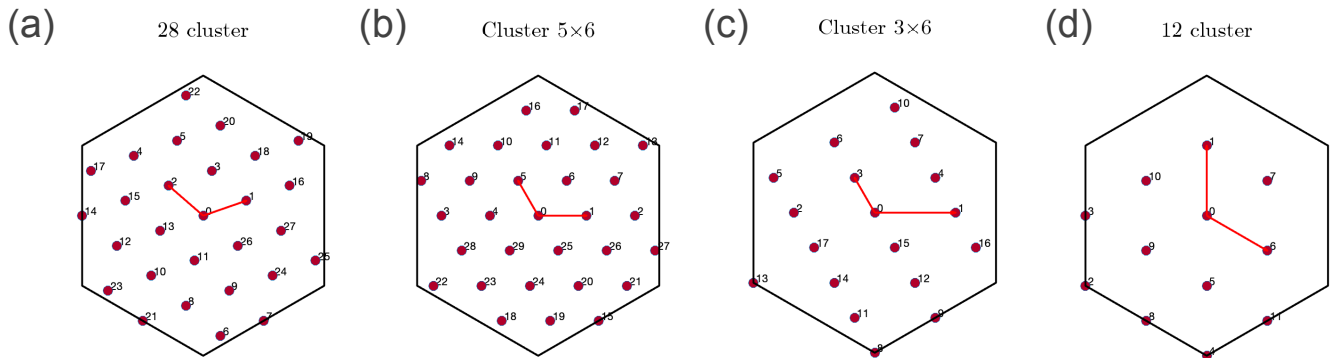


FIG. S3. The Finite-sized clusters we used in the ED calculations.

$s3p2d1$ denotes the inclusion of 3 sets of s -orbitals, 2 sets of p -orbitals, and 1 set of d -orbitals, totaling 14 atomic orbitals. Similarly, $Te7.0-s3p2d2$ includes 3 sets of s -orbitals, 2 sets of p -orbitals, and 2 sets of d -orbitals, amounting to 19 atomic orbitals. These configurations are used to perform the self-consistent calculations.

B. Chern number of top two band

Figure. S2(a) and S2(b) presents the distributions of Berry curvature. The Chern numbers, derived from the integral of Berry curvature, are calculated to be 1 for both the first and second bands. Additionally, gapless edge states are observed within the gaps between the first and second bands, as well as between the second and third bands. This phenomenon is explicitly depicted in Fig. S1(b), thereby affirming the nature of multiple Chern numbers within separate valleys.

C. The momentum geometry

We perform the ED calculation on the finite momentum cluster, which can be expressed with $\mathbf{k} = n_1\mathbf{t}_1 + n_2\mathbf{t}_2$, and n_1, n_2 are integers. Different geometries yield different values for \mathbf{t}_1 and \mathbf{t}_2 . In this study, we utilize two unnormal momentum cluster geometries: $\mathbf{t}_1 = (\mathbf{G}_{m1} + 2\mathbf{G}_{m2})/6$, $\mathbf{t}_2 = (\mathbf{G}_{m1} - \mathbf{G}_{m2})/6$ (Fig. S3(a)) and $\mathbf{t}_1 = (3\mathbf{G}_{m1} + \mathbf{G}_{m2})/14$, $\mathbf{t}_2 = (-\mathbf{G}_{m1} + 2\mathbf{G}_{m2})/14$ (Fig. S3(b)) and two other normal cluster geometry which we show in Fig. S3.

D. Other ED spectrum

In this part, we show the ED results on the 12-sites and 3x6 sites cluster, which displays two-fold quasi-degenerate states for the 12-site cluster (6 electrons) and six-fold degenerate states for 3x6 cluster (9 electron). Both the momentum and degeneracy agree with the predictions of the generalized Pauli principle. And it also reveals remarkable similarities with the 1stLL, as illustrated in Fig. S4.

E. The momentum counting from generalize Pauli principle

With the generalized Pauli principle for Moore-Read states, which means there is no more than two electron in four consecutive orbits, we calculate the momentum and degeneracy for the 28 sites and 30 sites cluster as we show in Fig. S5 and Fig. S6. For 30 sites, only the occupation partition “1010...101010” and its translational invariant partner “0101...010101” are allowed. And it also give the momentum 0 and 15 which agrees with our numerical results. With 28 sites, there are six possibilities denoted as Ψ_{gs1} through Ψ_{gs6} . Additionally, the calculation of the total momentum yields three pairs of states, each with a two-fold degeneracy, all of which match our exact diagonalization results.

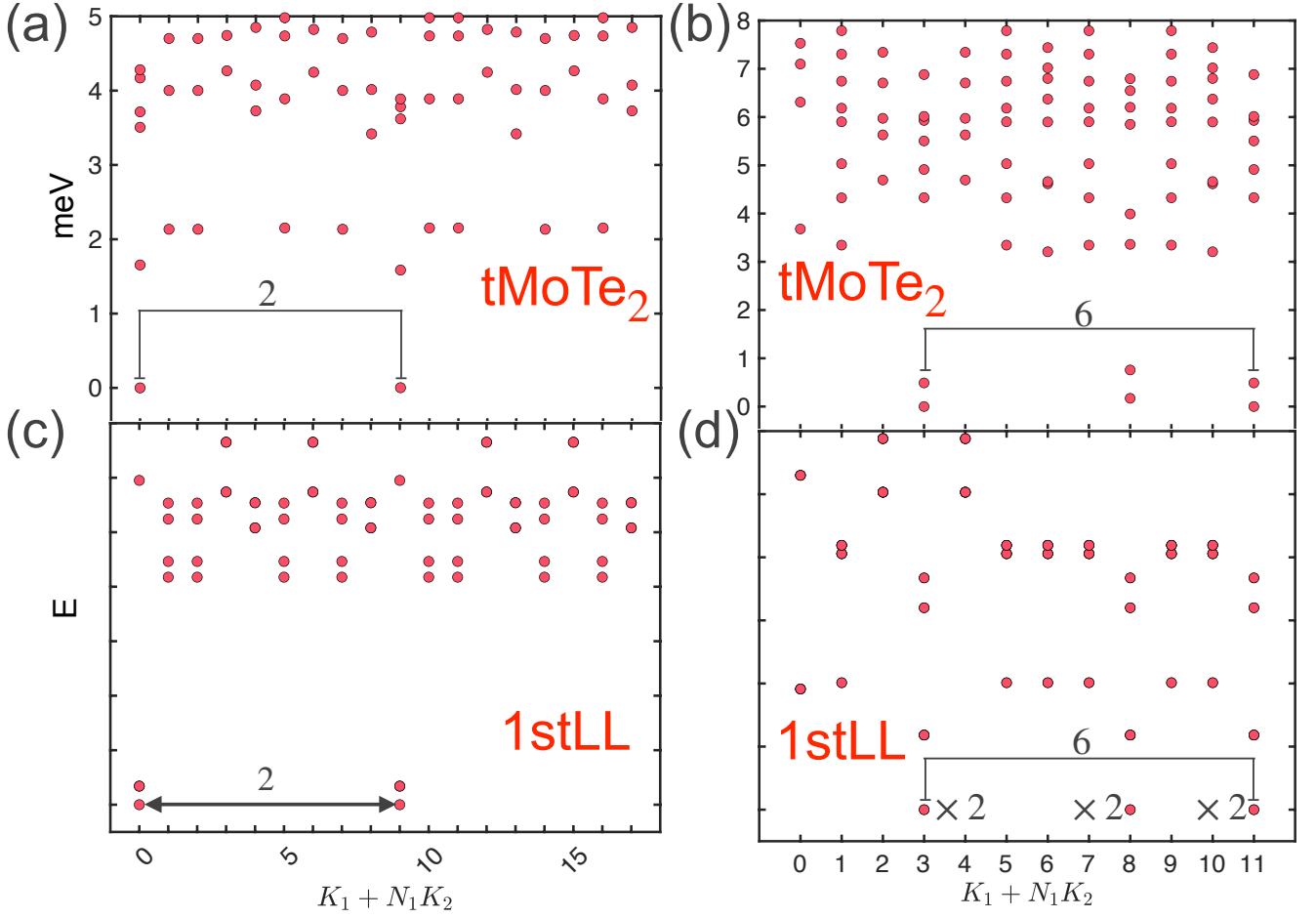


FIG. S4. Exact diagonalization spectrum. (a)/(b): the many-body spectrum from the ED calculation on the 18(12) cluster at filling factor $\nu = -\frac{3}{2}$ with the continuum model of MoTe₂ at $\theta = 2.0^\circ$ and we use the dielectric constant $\epsilon = 5$. And we use periodic condition for the 18 site cluster and anti-periodic condition for 12 site cluster. (c)/(d): the same calculation on the 1st Landau Level, which agrees well with our results from continuum model.

k_1	0	1	2	3	4	5	6	7	8	9	10	11	12	13	$\text{mod}(\sum k_i, N_i)$	$\text{mod}(\sum k_i, N_i)$	$k_1 + N_1 k_2$															
k_2	0	1	0	1	0	1	0	1	0	1	0	1	0	1																		
ψ_{gs1}	1	1	0	0	1	1	0	0	1	1	0	0	1	1	0	0	1	1	0	0	1	1	0	0	0	1	1	14				
ψ_{gs2}	0	1	1	0	0	1	1	0	0	1	1	0	0	1	1	0	0	1	1	0	0	1	1	0	0	1	1	0	7	1	21	
ψ_{gs3}	0	0	1	1	0	0	1	1	0	0	1	1	0	0	1	1	0	0	1	1	0	0	1	1	0	0	1	1	0	1	1	14
ψ_{gs4}	1	0	1	0	1	0	1	0	1	0	1	0	1	0	1	0	1	0	1	0	1	0	1	0	1	0	1	0	7	0	7	
ψ_{gs5}	1	0	0	1	1	0	0	1	1	0	0	1	1	0	0	1	1	0	0	1	1	0	0	1	1	0	0	1	7	1	21	
ψ_{gs6}	0	1	0	1	0	1	0	1	0	1	0	1	0	1	0	1	0	1	0	1	0	1	0	1	0	1	0	1	7	0	7	

FIG. S5. The counting that obeys the (2,4) admissible rule for 28 sites cluster as we show in Fig. S5.

k_2	0					1					2					3					4					5												
k_1	0	1	2	3	4	0	1	2	3	4	0	1	2	3	4	0	1	2	3	4	0	1	2	3	4	0	1	2	3	4	0	1	2	3	4	$\text{mod}(\sum k_i, N_i)$	$\text{mod}(\sum k_i, N_i)$	$k_1 + N_1 k_2$
ψ_{gs_1}	1	0	1	0	1	0	1	0	1	0	1	0	1	0	1	0	1	0	1	0	1	0	1	0	1	0	1	0	1	0	0	0	0					
ψ_{gs_2}	0	1	0	1	0	1	0	1	0	1	0	1	0	1	0	1	0	1	0	1	0	1	0	1	0	1	0	1	0	1	0	3	15					

FIG. S6. The counting that obeys the (2,4) admissible rule for 30 sites cluster as we show in Fig. S3(b).